ACSNANO

www.acsnano.org

ARTICLE

Oxygen Functionalized Copper Nanoparticles for Solar-Driven Conversion of Carbon Dioxide to Methane

Mohammadreza Esmaeilirad,[⊥] Alireza Kondori,[⊥] Boao Song, Andres Ruiz Belmonte, Jialiang Wei, Kamil Kucuk, Shubhada Mahesh Khanvilkar, Erin Efimoff, Wei Chen, Carlo U. Segre, Reza Shahbazian-Yassar, and Mohammad Asadi*

Cite This: *ACS Nano* 2020, 14, 2099–2108

Read Online

ACCESS | Metrics & More | Article Recommendations | Supporting Information

ABSTRACT: Solar conversion of carbon dioxide (CO_2) into hydrocarbon fuels offers a promising approach to fulfill the world's ever-increasing energy demands in a sustainable way. However, a highly active catalyst that can also tune the selectivity toward desired products must be developed for an effective process. Here, we present oxygen functionalized copper (OFn-Cu) nanoparticles as a highly active and methane (CH_4) selective catalyst for the electrocatalytic CO_2 reduction reaction. Our electrochemical results indicate that OFn-Cu (5 nm) nanoparticles with an oxidized layer at the surface reach a maximum CH_4 formation current density and turnover frequency of 36.24 mA/cm^2 and of 0.17 s^{-1} at the potential of −1.05 V *vs* RHE, respectively, exceeding the performance of existing Cu and Cu-based catalysts. Characterization results indicate that the surface of the OFn-Cu nanoparticles consists of an oxygen functionalized layer in the form of Cu^{2+} (CuO) separated from the underneath elemental Cu by a Cu^{+} (Cu_2O) sublayer. Density functional theory calculations also confirm that presence of the O site at the CuO (101) surface is the main reason for the enhanced activity and selectivity. Using this catalyst, we have demonstrated a flow cell with an active area of 25 cm^2 that utilizes solar energy to produce 7.24 L of CH_4 after 10 h of continuous process at a cell power density of 30 mW/cm^2.

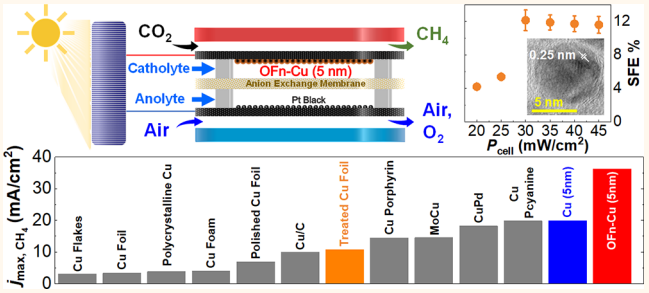

KEYWORDS: *CO_2 reduction, energy, solar-driven, copper, electrochemistry, in situ Raman, hydrocarbons*

Powering today's modernized society in a sustainable way motivates the development of alternatives to fulfill current and future energy needs that depend heavily on fossil fuels as the world's primary energy source.[1] Among various renewable energy sources, solar energy has a high potential to sustain energy needs due to its abundance, sustainability, and cost effectiveness. However, the intermittent nature of solar energy makes developing an efficient technology nearly impossible for this energy transformation.[2−4] One promising approach to resolve this issue is to store solar energy in the form of high-energy density fuels such as methane (CH_4), ethylene (C_2H_4), methanol (CH_3OH), and ethanol (C_2H_5OH).[5] Once this conversion happens through the CO_2 electrocatalytic reduction reaction, which recycles atmospheric CO_2 to usable chemicals using sunlight, it will also provide a sustainable solution to closing the carbon cycle.[6−15] However, using a catalyst that can minimize the input energy while boosting the product formation rate is crucial to make this process an effective competition for fossil fuels.

In this context, copper (Cu) and Cu-based catalysts are considered as promising candidates with the ability to form hydrocarbons.[16−22] Hydrocarbon products, such as CH_4, are preferred because they have a higher energy density (891.1 kJ mol^{-1}).[23] Moreover, they either can be utilized directly as a fuel or fed into various petrochemical/chemical processes to produce valuable chemicals and polymers. The overarching challenges of Cu and Cu-based catalysts are improving the activity and tuning the selectivity toward desired products. Recently, oxide-derived Cu has been shown to enhance the CO_2 reduction reaction performance metrics including selectivity, activity, and stability. More specifically, electrochemically oxide-derived μm-thick Cu_2O films have been

Received: November 6, 2019
Accepted: January 23, 2020
Published: January 23, 2020

https://dx.doi.org/10.1021/acsnano.9b08792
ACS Nano 2020, 14, 2099–2108

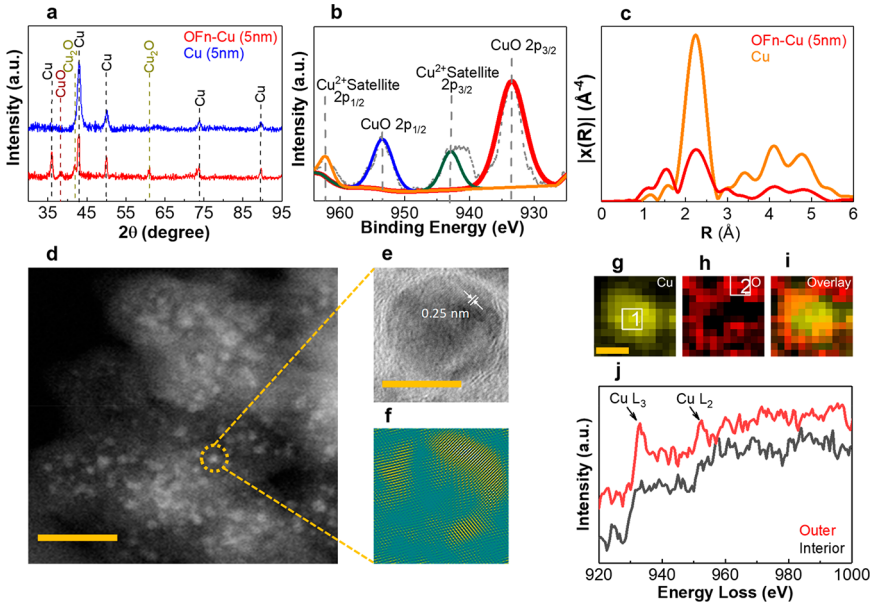

Figure 1. Structural and elemental analysis. (a) XRD patterns of OFn-Cu (5 nm) nanoparticles and Cu (5 nm) nanoparticles. (b) High-resolution X-ray photoelectron (HRXPS) spectrum of OFn-Cu (5 nm) nanoparticles. The HRXPS spectrum of the Cu 2p is fitted with standard CuO $2p_{1/2}$ and $2p_{3/2}$ peaks at 953.2 and 934.1 eV as well as standard Cu_2O $2p_{1/2}$ and $2p_{3/2}$ peaks at 952.5 and 932 eV, respectively. (c) EXAFS spectra of OFn-Cu (5 nm) nanoparticles and a Cu bulk standard. (d) Low-angle annular dark-field (LAADF-TEM) image of OFn-Cu (5 nm) on carbon black substrate (the scale bar is 20 nm). (e, f) HRTEM images of OFn-Cu (5 nm) nanoparticle (the scale bar is 5 nm). The outer region has a *d*-spacing of 0.25 nm that can be assigned to oxidized Cu plane. The oxidized Cu layer over the Cu core layer is highlighted. (g–i) EELS mapping of OFn-Cu (5 nm) with 5 Å spatial resolution (the scale bar is 2 nm), showing Cu K-edge, O K-edge, and overlaid EELS mapping. The oxidized layer covers the Cu nanoparticles. (j) EELS high-loss spectrum collected from regions 1 and 2 in (f).

demonstrated to catalyze the CO_2 reduction reaction to carbon monoxide (CO) and formic acid (HCOOH) with 40–50% faradaic efficiencies at low potentials (−0.3 to −0.6 V *vs* RHE) and C_2 products (C_2H_4 and C_2H_6) at high potentials (−0.6 to −0.95 V *vs* RHE) with faradaic efficiency (FE) of <10%.[17]

Here, we present oxygen-functionalized Cu (OFn-Cu) nanoparticles with an oxidized layer at the surface as a highly active and selective catalyst for CH_4 formation. Electrochemical results indicate that OFn-Cu (5 nm) nanoparticles have a maximum CH_4 formation FE of 60.6% and turnover frequency (TOF) of 0.17 s^{-1} at a low potential of −1.05 V *vs* RHE, outperforming existing Cu and Cu-based catalysts used for the same application.[17,19,24−27] The results of our characterization using high-resolution transmission electron microscopy (HRTEM), X-ray absorption spectroscopy (XAS), and X-ray photoelectron spectroscopy (XPS) confirm the existence of the oxygen functionalized layer in the form of Cu^{2+} (CuO) at the surface and Cu^{1+} (Cu_2O) as the sublayer of the synthesized catalysts. Our *in situ* Raman spectroscopy results also suggest that this oxidized layer remains stable and unchanged during the CO_2 electrocatalytic reduction reaction. Using OFn-Cu (5 nm) nanoparticles as the catalyst, we have also demonstrated a solar-powered flow cell that uses only solar energy, CO_2, and water-like buffer electrolyte (potassium bicarbonate) with a solar-to-methane efficiency and CH_4 formation rate of about 9% and 0.72 Lit/h, respectively, at the flow cell power density of 30 mW/cm^2 (equal to a cell potential of 2.2 V and photocurrent density of 13.63 mA/cm^2). Density functional theory (DFT) calculations reveal that CuO (101) and $(10\bar{1})$ surfaces have the lowest surface energies at 0.179 and 0.184 eV/$Å^2$, respectively. Moreover, the calculations indicate that all studied C_1 intermediates bind more strongly to the O site of the CuO (101) surface.

RESULTS AND DISCUSSION

A heterogeneous deposition–precipitation method followed by a thermal sintering process in a controlled oxygen/argon and hydrogen/argon environment was used to synthesize different particle sizes of OFn-Cu and Cu.[28−32] OFn-Cu and Cu nanoparticles were directly grown on the carbon black support using anchoring agents (section S1, Supporting Information). Figure 1a and Figure S1a,b (section S2, Supporting Information) show the X-ray diffraction (XRD) patterns of different sizes (1, 5, and 15 nm) of OFn-Cu on the carbon black substrate, Cu (5 nm) nanoparticles on the carbon black substrate and treated Cu foil (section S2, Supporting Information). The XRD pattern of Cu (5 nm) nanoparticles shows four broad peaks at 43.5°, 50.7°, 74.5°, and 90.4°, all of which are Bragg peaks of Cu (Figure 1a). In contrast, the XRD pattern of the synthesized OFn-Cu samples with Cu (5 nm) nanoparticles (Figure 1a and Figure S1a, section S2, Supporting Information) shows peaks at 42.4° and 61.6° due to the presence of Cu_2O and a weak reflection at 38.8° corresponding to the (101) plane of CuO. This result confirms the existence of the oxygen functionalized layer in the crystalline structure of the synthesized OFn-Cu samples. Additionally, the XRD patterns indicate the absence of other possible products such as $Cu(OH)_2$ and Cu_3O_4 (Figure 1a and Figure S1a, section S2, Supporting Information) for the synthesized OFn-Cu and Cu (5 nm) nanoparticles. The XRD results were used to measure a crystallite size of the synthesized OFn-Cu and Cu nanoparticles (Table S1, section S2, Supporting Information). Figure 1b shows the X-ray photoelectron spectroscopy result (XPS) of the fresh OFn-Cu (5 nm) nanoparticles. Comparing the result with the standard Cu 2p XPS spectra indicates CuO $2p_{1/2}$ and $2p_{3/2}$ peaks at 953.2 and 934.1 eV and Cu_2O peaks at 952.5 and 932 eV,

https://dx.doi.org/10.1021/acsnano.9b08792
ACS Nano 2020, 14, 2099−2108

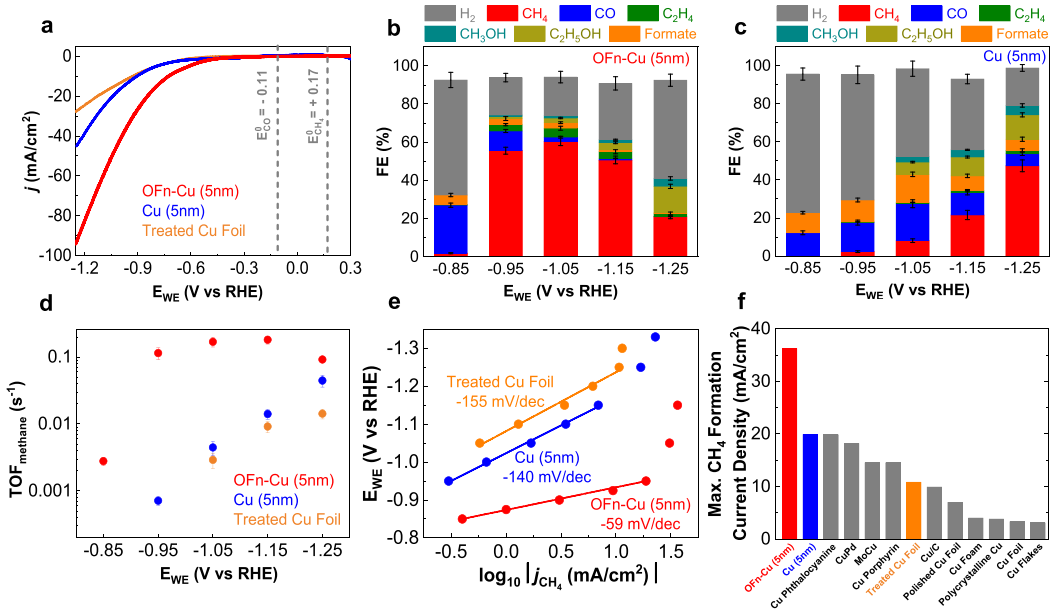

Figure 2. Electrochemical analysis of OFn-Cu (5 nm) nanoparticles, Cu (5 nm) nanoparticles, and treated copper foil catalysts for CO_2 reduction reaction. (a) LSV results for the studied catalysts with respect to RHE at a scan rate of 20 mV/s. (b, c) FE measurements for (b) OFn-Cu (5 nm) nanoparticles and (c) Cu (5 nm) nanoparticles at different applied potentials. Error bars are based on the standard deviation of four experiments at each potential. (d) CH_4 formation turnover frequency (TOF_{CH_4}) of studied catalysts at different applied potentials. Error bars are based on the standard deviation of four experiments at each potential. (e) Tafel plots (potential *vs* partial current density of CH_4 formation) measured for OFn-Cu (5 nm) nanoparticles, Cu (5 nm) nanoparticles, and treated Cu Foil. (f) Maximum CH_4 formation current density of Cu and Cu-based catalysts. The superior methane formation current density of OFn-Cu (5 nm) nanoparticles compared to the other Cu and Cu-based catalysts is also shown. All values are extracted from refs 17, 19, 24−27, and 47−49.

respectively, along with their corresponding satellite peaks. Our XPS analyses also show that the surface of the synthesized nanoparticles is mainly dominated by CuO (about 90 wt %), confirming the presence of an oxidized Cu layer in the form of Cu^{2+} (CuO) (section S3, Supporting Information).[18,33−35] Furthermore, XPS depth profiling of OFn-Cu (5 nm) suggests that the surface layer of the synthesized nanoparticles is dominated by CuO and separated from the elemental Cu underneath by a Cu_2O sublayer (Figures S3 and S4, section S3, Supporting Information). As shown in Figure S3b (section S3, Supporting Information), the surface of the fresh sample (not etched) is mostly composed of CuO (90% weight percentage) and a partial amount of Cu_2O which is mainly due to use of high temperatures in the thermal sintering step in catalyst preparation.[32,36−39] Additionally, as indicated in Figure S3b (section S3, Supporting Information), the XPS depth-profile results shows that the weight percentage of CuO decreases in the sublayers, dropping to 13.8% after argon etching of the surface for 2 nm where the weight percentage of Cu_2O and elemental Cu are 19.6% and 66.5%, respectively.

X-ray absorption spectroscopy (XAS) was used to characterize the structure of the synthesized catalysts (section S4, Supporting Information). Figures 1c and S6 show the magnitude of the Fourier transform of the extended X-ray absorption fine structure (EXAFS) spectra of the series of OFn-Cu samples compared with the standard EXAFS spectrum of Cu (Figure S5, section S4, Supporting Information). The peak at about 1.6 Å shows the presence of Cu−O bonds in increasing amounts as the nominal particle size decreases. The fits to these spectra confirm this increase along with a corresponding decrease in the number of Cu−Cu near neighbors characteristic of elemental Cu as the particle size is reduced from 15 to 1 nm. These results were also used to estimate the size of the elemental Cu core for the OFn-Cu nanoparticles with the additional information on the atomic fraction of Cu that resides in the core (section S4.2, Supporting Information). These data were extracted from the X-ray absorption near edge structure (XANES) by least-squares fitting of the derivative of the XANES to standard spectra of Cu, Cu_2O, and CuO (Figure S7 and Table S3, Supporting Information). The spectra of OFn-Cu samples show an increasing atomic fraction of Cu−O with decreasing size of particles, suggesting the existence of an oxidized layer surrounding the Cu elemental cores.

We also performed high-resolution transmission electron microscopy (HRTEM) to characterize the structural properties of synthesized OFn-Cu (5 nm), as shown in Figure 1d−j with different scales (section S5, Supporting Information). Figure 1d shows the low-angle annular dark-field (LAADF) image of the well-dispersed OFn-Cu (5 nm) nanoparticles, confirming spherical shape and uniform size distribution for the OFn-Cu nanoparticle synthesized on the carbon black support. Figure 1e shows a HRTEM image of a single OFn-Cu (5 nm) nanoparticle. The outer region has a *d*-spacing of 0.25 nm which can be assigned to the oxidized Cu (Cu^{2+}) layer.[40−42] By masking the diffraction from the oxidized Cu layer and performing inverse FFT, this layer is highlighted in Figure 1f. The electron energy loss spectroscopy (EELS) analysis for OFn-Cu (5 nm) was performed using 5 Å spatial resolution focused on a single nanoparticle (Figures 1g−i). Figure 1g−i shows the oxidized copper layer covers the Cu nanoparticle. Furthermore, EELS spectrum from regions 1 and 2 in Figure 1g,h related to Cu interior and oxidized layer are extracted and shown in Figure 1j. It is well-known that pristine Cu does not show a white-line feature in the near-edge fine structure (ELNES) of the $L_{2,3}$ edge due to a fully occupied d-band, and

https://dx.doi.org/10.1021/acsnano.9b08792
ACS Nano 2020, 14, 2099−2108

the white-line feature serves as sensitive measurement of Cu oxidation. Comparing the EELS spectrum from regions 1 and 2 in Figure 1g,h, the outer shell region shows a sharper $L_{2,3}$ white-line which is due to the existing oxidized Cu layer. The size analysis of OFn-Cu nanoparticles by TEM results also indicates an average particle size of about 5 nm for OFn-Cu (5 nm) that is consistent with our EXAFS and XRD results (Figures S8 and S10, section S5, Supporting Information).

Next, we studied the catalytic performance of OFn-Cu nanoparticles for an electrocatalytic CO_2 reduction reaction in a custom-designed sealed two-compartment three-electrode electrochemical cell (Figure S11, section S6, Supporting Information). All electrochemical experiments were performed under identical conditions in 1 M $KHCO_3$ electrolyte saturated with CO_2, where the pH of the saturated electrolyte was measured before and after experiments. The results indicated that pH value remained almost constant at about 8 (section S6, Supporting Information). The linear sweep voltammetry (LSV) test is performed for different sizes of OFn-Cu nanoparticles ranging from 1 to 15 nm, Cu (5 nm) and treated Cu foil, by a sweeping voltage from +0.3 V to −1.25 V *vs* RHE (all potentials in this study are presented with respect to reversible hydrogen electrode, eq S3, section S6, Supporting Information) with a scan rate of 20 mV/s. Figure 2a shows the LSV results of OFn-Cu (5 nm) nanoparticles compared to Cu (5 nm) and treated Cu foil, a commonly used catalyst for CO_2 reduction reaction. The LSV results of OFn-Cu (1 nm) and OFn-Cu (15 nm) also are presented in Figure S12 (section S6, Supporting Information). Current densities in Figures 2a and S12 are reported based on the geometrical surface area of the working electrode using 1 cm^2 glassy carbon electrodes as the substrate. The LSV results shown in Figures 2a and S12 indicate that the current density of −10 mA/cm^2 can be achieved at overpotentials ($\eta_{-10\ mA/cm^2}$) of 708, 723, and 826 mV for 1, 5, and 15 nm OFn-Cu nanoparticles, respectively, where Cu (5 nm) nanoparticles and treated Cu foil exhibits $\eta_{-10\ mA/cm^2}$ of 904 and 923 mV, respectively. At a potential of −1.05 V, the recorded current density for 1 nm OFn-Cu is −70.2 mA/cm^2, which is 1.4, 2, 3.4, and 4.4 times higher than that observed for 5 nm OFn-Cu (−51.1 mA/cm^2), 15 nm OFn-Cu (−34.4 mA/cm^2), 5 nm Cu (−20.8 mA/cm^2), and treated Cu foil (−15.9 mA/cm^2), suggesting an overall higher activity of OFn-Cu nanoparticles compared to Cu (5 nm) and treated Cu foil.

We evaluated the selectivity of synthesized OFn-Cu nanoparticles in the same electrochemical cell. The product stream analysis was performed using gas chromatography (GC), *in situ* differential electrochemical mass spectrometry (DEMS) for gas-phase products, and nuclear magnetic resonance (NMR) spectroscopy for liquid-phase products (section S7, Supporting Information). Figures 2b,c and S14 (section S7, Supporting Information) show FE results of different sizes of OFn-Cu nanoparticles compared with the Cu (5 nm) and treated Cu foil. As shown in Figures 2b,c and S14, the CH_4 and C_2H_4 formation potential is about −0.85 V for OFn-Cu nanoparticles (section S7, Supporting Information). However, CH_4 is formed at a potential of −1.05 V with FE of 8.12% and 3.82% for the Cu (5 nm) and treated Cu foil, respectively, where OFn-Cu (5 nm) showed the maximum CH_4 formation FE of 60.6% at this potential. Furthermore, the highest CH_4 formation FEs of 43.11% and 54.79% are calculated for OFn-Cu (1 nm) and OFn-Cu (5 nm) at a potential of −1.05 V (Figure S14, section S7, Supporting Information). At a potential of −1.05 V, the OFn-Cu (5 nm) nanoparticles exhibit C_2H_4, CH_3OH, C_2H_5OH, and formate FEs of 4.72%, 1.2%, 2.41%, and 2.91%, respectively (Table S4, section S7, Supporting Information). The FE measurement results also show that different sizes OFn-Cu nanoparticles (1−15 nm) are mainly selective for CH_4 formation in a potential range of −0.95 to −1.15 V with CO, C_2H_4, CH_3OH, C_2H_5OH, formate, and H_2 formed as the other products in this process (section S7, Supporting Information). The results for OFn-Cu (5 nm) nanoparticles shown in Figure 2b indicate an overall FE of 94.12% ± 6 (87.58% gas products and 6.54% liquid products) at a potential of −1.05 V. The $^{13}CO_2$ isotope experiments also confirm that the CO_2 gas present inside the electrolyte is the only source of the formed products in the CO_2 reduction reaction (section S8, Supporting Information).

We evaluated the intrinsic catalytic activity of the studied catalysts toward CH_4 formation by calculating corresponding TOFs presenting actual CH_4 formation performance per catalytic active site using the roughness factor (RF) method (section S9, Supporting Information).[43,44] For all the studied catalysts, the TOFs are normalized to the number of active sites on a surface area of 1 cm^2. Figures 2d and S20 (section S9, Supporting Information) indicate that the OFn-Cu (5 nm) catalyst shows a maximum CH_4 formation TOF of 0.17 s^{-1} at a potential of −1.05 V which is 2.96 and 1.76 times higher than OFn-Cu (1 nm) and OFn-Cu (15 nm) nanoparticles. The measured CH_4 formation TOF of OFn-Cu (5 nm) catalyst at −1.05 V is 42- and 56-fold higher than the Cu (5 nm) nanoparticles (0.00446 s^{-1}) and treated Cu foil (0.00291 s^{-1}), confirming the superior CH_4 formation performance for the OFn-Cu (5 nm) nanoparticles compared to other studied catalysts in this work.

The kinetic studies were also evaluated using Tafel plots, that is, partial current densities of the different products as a function of the potential for OFn-Cu (5 nm), treated Cu foil, and Cu (5 nm) nanoparticles (Figures 2e and S21, section S10, Supporting Information). As shown in Figure 2e, the CH_4 formation Tafel slope of about −59 mV/dec observed for OFn-Cu (5 nm) is much lower than that of the Cu (5 nm) nanoparticles (−140 mV/dec) and treated Cu foil (−155 mV/dec), indicating a faster reaction kinetics toward CH_4 formation for OFn-Cu (5 nm). The observed Tafel slope of −59 mV/dec in the low current density region for CH_4 formation using OFn-Cu (5 nm) suggests that the CHO/COH intermediate formation through CO hydrogenation process is the rate-determining step.[24,45,46] Moreover, the lower Tafel slopes of OFn-Cu (5 nm) for CH_4 (−56 mV/dec), C_2H_4 (−32 mV/dec), and formate (−157 mV/dec) compared with CO (−200 mV/dec) indicate faster reaction kinetics toward hydrocarbon formation.

We also compared the maximum CH_4 formation current density for OFn-Cu (5 nm) nanoparticles with other Cu and Cu-based catalysts[17,19,24−27,48,49] as well as Cu (5 nm) nanoparticles and treated Cu foil. The results shown in Figure 2f indicate the maximum CH_4 formation current density of OFn-Cu (5 nm) nanoparticles (36.24 mA/cm^2) is 1.82, 1.83, 2, 2.5, and 3.5 times higher than Cu (5 nm) nanoparticles, Cu(II) phthalocyanine,[17] CuPd,[26] MoCu,[48] and treated Cu foil, respectively, confirming the superior CH_4 formation activity of OFn-Cu (5 nm) nanoparticles compared to other Cu and Cu-based catalysts.

To determine the oxidized layer stability of OFn-Cu (5 nm) nanoparticles under electrochemical CO_2 reduction reaction, *in*

https://dx.doi.org/10.1021/acsnano.9b08792
ACS Nano 2020, 14, 2099−2108

situ Raman spectroscopy of the catalyst surface was performed at an applied potential of −1.05 V in a custom designed cell (Figure S24, section S11, Supporting Information). Figure 3

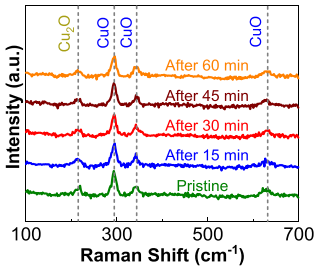

Figure 3. *In situ* Raman measurement of the cathode coated with OFn-Cu (5 nm) nanoparticles during an electrochemical CO_2 reduction reaction at a potential of −1.05 V in the custom designed cell (Figure S23, section S11, Supporting Information). Raman spectra were obtained at different time intervals of 15 min.

shows the recorded Raman spectra of OFn-Cu (5 nm) nanoparticles from 100 to 700 cm^{-1} at time intervals of 15 min. As shown in this figure, the Raman spectrum of pristine cathode coated with OFn-Cu (5 nm) nanoparticles shows peaks at 213.52 cm^{-1} (Cu_2O), 295 cm^{-1} (CuO), 341.77 cm^{-1} (CuO), and 631.08 cm^{-1} (CuO). The Raman spectra of the cathode surface at different time intervals shown in Figure 3 do not suggest any noticeable change in the observed peaks after 1 h of CA experiment at −1.05 V.

We also studied the stability of OFn-Cu (5 nm) nanoparticles by performing chronoamperometry (CA) experiments at different potentials followed by XPS characterization of the surface after CA experiment (Figures S25, Supporting Information). The results suggest that the weight percentages of the composition at the surface of catalyst (CuO, Cu_2O and Cu) remain fairly unchanged after CA experiment. The scanning electron microscopy (SEM) results of the cathode surface before and after the electrochemical CO_2 reduction reaction also indicate a similar surface morphology before and after the CA experiments (Figure S27, section S12, Supporting Information). These results confirm the stability of oxidized layer during the electrochemical CO_2 reduction reaction.

To gain more insight into the origin of the CO_2 reduction reaction activity in the synthesized catalysts, we compared the surface work function for OFn-Cu (5 nm) nanoparticles using ultraviolet photoelectron spectroscopy (UPS) method (section S13, Supporting Information).[50] The UPS measurements indicate that the surface work function of 4.29 eV for OFn-Cu (5 nm) sample (Figure S28, section S13, Supporting Information) is 0.2 and 0.58 eV lower than those of Cu (5 nm) and treated Cu foil, respectively, suggesting an easier electron transfer and higher catalytic activity for OFn-Cu (5 nm) nanoparticles.

Next, we tested the CO_2 reduction reaction catalytic performance and energy efficiency of the OFn-Cu (5 nm) nanoparticles in a solar-driven two-compartment electrochemical flow cell containing an active surface area of 25 cm^2 at the cathode and anode sides of the cell (section S14, Supporting Information). The flow cell was powered by a triple junction photovoltaic (TJ-PV) cell with a maximum efficiency of 34.32% (section S14, Supporting Information). Figure 4a shows the $j-V$ characteristic curve (red curve) of the TJ-PV cell under one sun illumination (100 mW/cm^2) using a sun

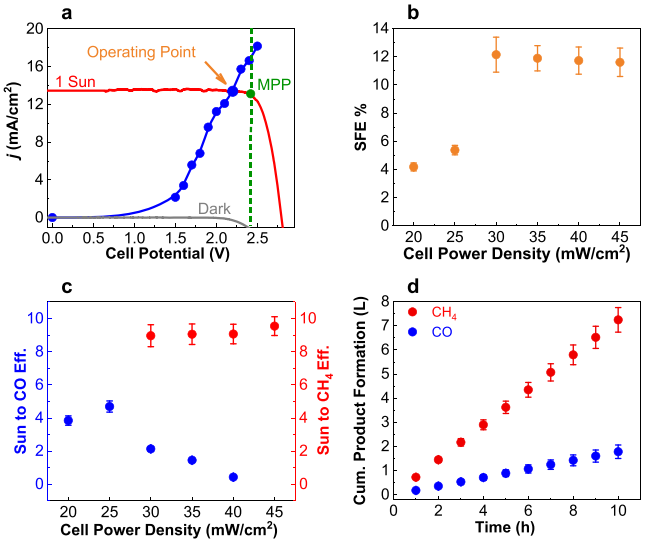

Figure 4. Electrochemical analysis of OFn-Cu (5 nm) nanoparticles in the solar-driven flow cell. (a) Characteristic curve (shown in red) of the TJ-PV cell under 1 sun illumination. The blue curve shows the measured current density at different cell potentials obtained by chronoamperometry results (Figure S30, section S14, Supporting Information). The maximum power point (MPP) indicating a current density of 13.2 mA/cm^2 at the cell potential of 2.42 V is shown in this figure. (b) Overall SFE (including CH_4, CO, C_2H_4, CH_3OH, C_2H_5OH, and formate) of the solar-driven flow cell at different flow cell powers. The error bars indicate overall uncertainty in the calculated SFE values shown in this figure (section S12.2, Supporting Information). Error bars corresponding to SFEs are 0.2931 and 0.3487 at cell power densities of 20 and 25 mW/cm^2, respectively. (c) Measured solar to CH_4 and CO formation efficiency of the solar-driven flow cell under 1 sun illumination at different flow cell powers (section S13, Supporting Information). Uncertainty analysis is performed to calculate error bars for the sun to CO and CH_4 formation efficiency values shown in this figure (section S12.2, Supporting Information). Error bars corresponding to sun to CO formation efficiencies are 0.2811, 0.3358, 0.1359, 0.0880, and 0.0249 at cell power densities of 20, 25, 30, 35, and 40 mW/cm^2, respectively. (d) Cumulative CH_4 and CO formation over 10 h of continuous process.

simulator light source (section S15.1, Supporting Information). The blue curve shown in Figure 4a presents the measured current density (CA results) of the flow cell at different applied potentials (Figure S30, section S14, Supporting Information). The optimum operating point for the coupled system is determined by the point at which the two curves intersect (Figure 4a). At the optimum operating point (section S15, Supporting Information), a maximum photocurrent density of 13.63 mA/cm^2 is obtained using 1 sun illumination at a cell potential of −2.2 V. This results in an overall energy efficiency of 29.5% for the TJ-PV cell which is relatively close to its maximum efficiency.

Using this setup, solar to fuel (CH_4, CO, C_2H_4, CH_3OH, C_2H_5OH, and formate) efficiencies (SFEs) were measured during the continuous electrocatalytic conversion of CO_2 at different flow cell power density supplied by the TJ-PV cell (Figure 4b, section S15.1, Supporting Information). To do this, the TJ-PV cell was calibrated to generate the required photocurrent at various cell potentials (−2 to −2.5 V) for the CO_2 reduction reaction by varying its surface area (Figure S35, section S15, Supporting Information). Figure 4b presents the

https://dx.doi.org/10.1021/acsnano.9b08792
ACS Nano 2020, 14, 2099−2108

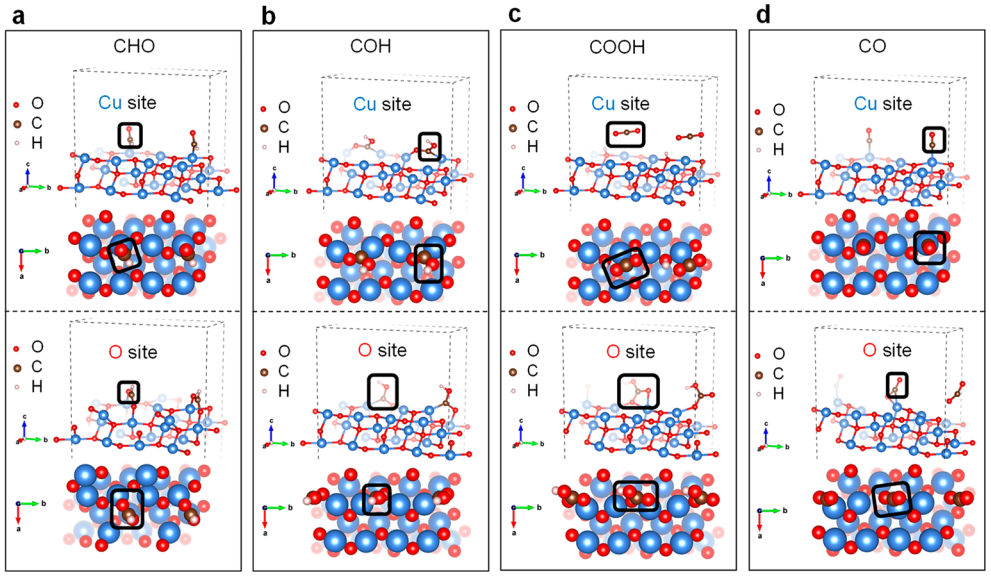

Figure 5. Adsorption of (a) CHO, (b) COH, (c) COOH, and (d) CO on CuO (101) surface at the Cu site and O site. Species adsorbates are highlighted with a black line square.

total SFE of the developed electrochemical device. The results show that the maximum SFE of 12.15% is obtained at a flow cell power density of 30 mW/cm^2, while it decreases to about 11.6% at a power density of 45 mW/cm^2. This confirms the power density of 30 mW/cm^2 as the most effective operation power density with solar to CH_4, CO, C_2H_4, CH_3OH, C_2H_5OH, and formate efficiencies of about 8.97, 2.13, 0.27, 0.13, 0.22, and 0.42%, respectively (Figure S36, section S15.1, Supporting Information).

The results (Figure 4c) show about 9% solar to CH_4 formation efficiency at a flow cell input power density of 30 mW/cm^2, which increases slightly (9.54%) by increasing the cell input power density to 45 mW/cm^2. However, the highest solar to CO formation efficiency of 4.69% is obtained at a flow cell power density of 25 mW/cm^2.

The long-term performance of the solar-driven flow cell was also evaluated at a power density of 30 mW/cm^2 (Figure 3d and Figure S37, section S15.3, Supporting Information). Figure 4d shows the cumulative product formation during the continuous process of the CO_2 reduction reaction powered by the solar cell. These results illustrate that approximately 7.24 and 1.78 L of CH_4 and CO were produced, respectively, during a 10 h run at the optimal operating power density of 30 mW/cm^2. As shown in Figure S37a (section S15, Supporting Information), an average value of 8.73% was measured for solar to CH_4 formation efficiency under 1 sun illumination with negligible variation (about 3%) over 10 h of continuous process, confirming the high stability of the OFn-Cu (5 nm) nanoparticles used for CO_2 reduction reaction in the solar-driven flow cell (Figure S37b, section S15.3, Supporting Information).

Finally, we performed a computational study to calculate the surface energy and work function for several low-index surface terminations of CuO (Table S7, section S16, Supporting Information). Among the studied CuO terminations, the (101) and $(10\bar{1})$ surfaces have the lowest surface energies at 0.179 and 0.184 eV/Å^2, respectively. These two surfaces are also among the terminations with the lowest work functions at 5.268 and 5.152 eV, respectively.

Adsorptions of possible C_1 intermediates on different sites of the CuO (101) surface have also been studied to identify the preferred adsorption site. To do this, we analyzed the optimized adsorption structures on the CuO (101) surface. The calculation results show that the preferred adsorption to the O site is particularly strong for CHO, where the difference in adsorption energy between the Cu and O sites is almost 1.5 eV. Figure 5a also shows that the stable CHO adsorption site is the hollow site next to the surface O atom, where a new bond is formed between the O atom of CHO and the neighboring Cu atom on the CuO (101) surface. This is similar to previous studies on Rh (111)[51,52] where the CHO intermediate formed through CO hydrogenation exhibits a lower barrier.[42] However, for the COH intermediate, the adsorption energy is much more negative for both the Cu and O sites, suggesting COH as a likely intermediate[43] which is also consistent with our kinetic study using a Tafel plot (Figure 2e).

Figure 5b shows surface reconstructions that can be observed after COH adsorption. As shown in this figure, adjacent surface O atoms are lifted from the surface plane by the C atoms in COH. The most stable site for COH adsorption is the bridge site of CuO (101) (Figure S38, section S16, Supporting Information). Lastly, the adsorption of COOH at the O site is similar to the CHO adsorbed at the O site, where new bonds formed between the O atoms in COOH and the neighboring surface Cu atoms. COOH dissociates spontaneously to H and O−C−O when it is adsorbed at the Cu site of CuO (101), as shown in Figure 5c. The surface layers of CuO (101) behave distinctively when adsorption takes place at different sites. When adsorbed at the Cu site, the surface layer does not relax much except for the COH adsorbates. However, we observed surface Cu−O cleavage and new bond formation between adsorbate and Cu atom at CuO (101) when adsorbed at the O site for CO, CHO, and COOH. For instance, the surface Cu−O bond length is 1.863 Å before adsorption. After CO adsorption at the O site, the surface Cu−O bond breaks, and C forms a new bond with the neighboring Cu ion with a bond length of about 2 Å.

https://dx.doi.org/10.1021/acsnano.9b08792
ACS Nano 2020, 14, 2099−2108

The adsorption energies of studied intermediates, that is, CHO, COH, COOH, and CO on the CuO (101) surface are listed in Table S8 (section S16, Supporting Information). The calculations indicate that all studied C_1 intermediates bind preferentially to the O site of the CuO (101) surface where the adsorption of COH and CO is the strongest and the weakest, respectively. The results also indicate that the formation of a new bond as well as the cleavage of a surface Cu−O bond are the two key factors stabilizing the O site adsorption.

CONCLUSIONS

In summary, we have synthesized different sizes of OFn-Cu nanoparticles (1−15 nm) using a scalable and facile colloidal chemistry technique and tested these nanoparticles for the electrocatalytic CO_2 reduction reaction. The LSV and FE measurement results indicate that the catalytic activity and the selectivity of the OFn-Cu nanoparticles having oxidized layer at the surface exceed that of Cu nanoparticles and treated Cu foil. The performance of the OFn-Cu (5 nm) was also evaluated in a two-compartment flow cell for continuous electrocatalytic reduction of CO_2 at different cell potentials. The electrochemical results revealed that the maximum CO_2 reduction reaction efficiency was obtained at −2.2 V with CH_4, CO, C_2H_4, CH_3OH, C_2H_5OH, and formate formation FEs of 51, 12, 1.54, 0.63, 1.07, and 3.2%, respectively. By coupling the two-compartment flow cell with a TJ-PV cell, we developed a stand-alone solar-powered prototype that effectively converts CO_2 to CH_4 with a SFE of about 9% at a power density of 30 mW/cm^2 (cell potential of −2.2 V and current density of 13.63 mA/cm^2). We also performed extensive atomic-scale characterizations such as XRD, EXAFS, XANES, HRTEM, XPS, and *in situ* Raman to elucidate the physical properties and stability of the OFn-Cu (5 nm), revealing that the oxidized layer is in the form of Cu^{2+} (CuO) at the surface and Cu^{1+} (Cu_2O) at the sublayer of the OFn-Cu (5 nm) nanoparticles. DFT calculation results also reveal that the presence of O sites at the CuO (101) surface is a key factor for making this catalyst selective for CH_4 formation. The demonstrated solar-powered electrocatalytic CO_2 reduction reaction in this study can potentially be employed as an effective way to power our current and future energy needs in a sustainable way.

METHODS

Materials Preparation. Copper(II) nitrate trihydrate [$Cu(NO_3)_2.3H_2O$] (Sigma-Aldrich), carbon black (Fuel Cell store), and sodium hydroxide [NaOH] (Sigma-Aldrich) were used in the heterogeneous −precipitation (DP) method for the synthesis of OFn-Cu nanoparticles. The nitrate solution of copper (Cu) was prepared by adding 50 mL of deionized water to 670 mg of Cu salt. The DP process was conducted for 12 h on a magnetic hot plate at 90 °C. Metal ions were precipitated on 1.1 g of carbon black by adding 40 mL of 6 wt % NaOH solution in specific time intervals to obtain different sizes of Cu nanoparticles with 16 wt % metal loading deposited on the carbon black. The solution containing the so-called Cu nanoparticles was then washed with deionized water, filtered, and dried in a vacuum oven at 110 °C overnight. The dried powders were ground and subsequently functionalized in a tubular furnace using a mixed oxygen/argon (O_2/Ar) flow with the volume ratio of O_2:Ar 1:9 under a pressure of 100 Torr for 4 h at 500 °C. In addition, Cu 5 nm nanoparticles deposited on carbon black were synthesized using the same DP method. However, instead of an O_2/Ar gas mixture, a mixed flow of argon/hydrogen (Ar/H_2) with 8% concentration of H_2 was used in the tubular furnace for the thermal sintering step. A specific amount of obtained catalyst was then dispersed in 2-propanol and then coated on a glassy carbon electrode for the electrochemical experiments.

Characterization Techniques. XRD patterns were collected by a Bruker D2 PHASER diffractometer in Bragg−Brentano geometry employing Ni filtered Cu Kα radiation. XRD patterns were obtained from 30 to 100° 2θ degree using a LynxEye linear position-sensitive detector. A step width of 0.2° 2θ and a counting time of 10 S/step were used. XPS of OFn-Cu (5 nm) was obtained using a Thermo-Scientific ESCALAB 250Xi instrument equipped with an electron flood and scanning ion gun. Obtained spectra were all calibrated to the C 1s binding energy at 284.8 eV. Thermo-Advantage software was used to quantify the precise atomic concentration of each element within the sample. EXAFS spectra were taken on the nominal 15, 5, and 1 nm samples in transmission at the Materials Research Collaborative Access Team (Sector 10) bending magnet beamline at the Advanced Photon Source of Argonne National Laboratory.[53] A small amount of sample was ground in a mortar with boron nitride and PVDF and then pressed into a 7 mm pellet. EXAFS data analysis was performed using the Athena and Artemis programs from the IFEFFIT suite.[54,55] The morphology and particle size distribution of OFn-Cu (5 nm) catalyst were measured using a spherical aberration-corrected JEOL JEM-ARM 200CF TEM with a cold field emission gun operating at 200 kV, with 22 mrad convergence angle. The *in situ* Raman spectroscopy was carried out using Horiba LabRAM HR Evo Confocal Raman (Horiba Scientific Instrument, US). A 532 nm laser source, a Horiba Synapse detector, 600 g/mm grating, and a long-distance 50× objective were used to probe the samples.

Electrochemical Measurements. A custom-designed two-compartment three-electrode electrochemical cell with 1 M $KHCO_3$ electrolyte saturated with CO_2 (UHP 99.99%, Airgas) was used to perform the LSV, CV, and CA experiments. The synthesized catalysts were coated by a drop casting method on a glassy carbon electrode that was later used as the working electrode. The catalyst loading on the electrode was precisely controlled to be 0.1 mg on the glassy carbon electrode with the surface area of 1 cm^2. Platinum (Pt) gauze 52 mesh (Alfa Aesar) and Ag/AgCl (BASi) were used as counter and reference electrodes, respectively. The cathode and anode parts of the cell were separated through an ion exchange membrane (Nafion 212, Fuel Cell Store) to eliminate the effect of product oxidation at the anode surface. The pH of the electrolyte was measured before and after the experiments using a Thermo Scientific Orion A111 pH meter. The results indicate that the pH value remained almost constant (about 8.0) before and after the CO_2 reduction reaction. The cell was connected to the potentiostat (SP 150 Biologic) for the electrolysis experiments.

In addition, the electrocatalytic activity of OFn-Cu (5 nm) as the cathode, platinum black nanoparticles as the anode, and the 1 M $KHCO_3$ electrolyte was studied in a two-compartment electrochemical flow cell. Figure S29 (section S14, Supporting Information) shows the schematic of the flow cell setup with a total space volume of 60 mL, where two 1 cm-thick polypropylene sheets with a 5 cm × 5 cm window are placed between two gas diffusion layers GDLs, and there is an ionic exchange membrane (Selemion, AGC Engineering Co.) to separate the catholyte (30 mL volume) and anolyte (30 mL volume). The membrane was sonicated in deionized water water for 30 min at 80 °C and dried over N_2 to clean the surface prior to use. The exposed geometric active area of the cell is 25 cm^2. The electrolyte was continuously pumped through the chambers of the electrochemical flow cell with constant flow rate of 25 mL/min.

For the standalone self-operating process, the two-compartment electrochemical flow cell was connected to a triple junction photovoltaic (TJ-PV) cell to power the two-compartment electrochemical flow cell with solar energy (section S12, Supporting Information). The TJ-PV cell was characterized at different sun illuminations by connecting to the potentiostat.

A gas chromatography system (SRI 8610C Multiple Gas Analyzer), differential electrochemical mass spectrometer (DEMS, HPR-40, Hiden Analytical), and ^1H nuclear magnetic resonance spectroscopy (500 MHz Bruker Advance III HD system) were used to analyze the

https://dx.doi.org/10.1021/acsnano.9b08792
ACS Nano 2020, 14, 2099−2108

gas-phase and liquid-phase products of the electrochemical experiments (section S7, Supporting Information).

Computational Studies. First-principles calculations were performed using the projector augmented-wave method as implemented in the Vienna *ab Initio* Simulation Package.[56] The exchange−correlation energy was approximated using the generalized gradient approximation with the Perdew−Burke−Ernzerhof parametrization.[44] The optimized bulk CuO structure was retrieved from the Materials Project.[57] Surface energy and work function were then calculated for low-index surfaces of CuO.[58] The slab models for these surfaces contain at least 15 Å of atomic layers and vacuum spacing, where all layers could relax during the surface-energy calculations. Adsorption of selected C_1 products (CO, CHO, COH, and COOH) was calculated on the CuO (101) surface, with the lowest-energy surface termination studied. The CuO (101) slab was composed of nine layers of four Cu and O atoms. The adsorption was considered at both the Cu and O sites of the CuO (101) surface to study the preferred adsorption site at the 1 ML coverage (in terms of surface Cu atoms). During the adsorption calculations, the top three atomic layers and adsorption products could relax. All calculations were initialized with high spin polarization, and the cutoff energy for the plane wave expansion was 520 eV. A 2 × 2 × 1 γ-centered *k*-point mesh was used for slab calculations. The energy and force criteria for slab relaxation were 1×10^{-3} eV/atom and 0.02 eV/ Å. The equilibrium morphology of CuO particles is predicted by constructing a Wulff shape with the surface energy values in Table S7. The prevailing surfaces of the Wulff shape are the (101) surface, which constitutes 27% of the particle surface area, followed by the $(10\bar{1})$ surface at 26%.

ASSOCIATED CONTENT

Supporting Information

The Supporting Information is available free of charge at https://pubs.acs.org/doi/10.1021/acsnano.9b08792.

> Additional details on synthesis and preparation of the studied catalysts (OFn-Cu NPs, Cu NPs, treated Cu foil), characterization techniques including XRD, XPS, XAS, EXAFS, XANES, Raman, SEM, and HRSTEM analysis of the catalysts, three-electrode cell and two-compartment flow cell for electrochemical CO_2 reduction reaction experiments, product analysis and faradaic efficiency measurements, isotope ^{13}C CO_2 experiment, TOF calculations, SFE measurements, uncertainty analysis of the SFE calculation as well as computational methods (PDF)

AUTHOR INFORMATION

Corresponding Author

Mohammad Asadi − *Department of Chemical and Biological Engineering, Illinois Institute of Technology, Chicago, Illinois 60616, United States;* orcid.org/0000-0003-0354-2473; Email: m.asadi@iit.edu

Authors

Mohammadreza Esmaeilirad − *Department of Chemical and Biological Engineering, Illinois Institute of Technology, Chicago, Illinois 60616, United States;* orcid.org/0000-0002-1575-2892

Alireza Kondori − *Department of Chemical and Biological Engineering, Illinois Institute of Technology, Chicago, Illinois 60616, United States*

Boao Song − *Department of Mechanical and Industrial Engineering, University of Illinois at Chicago, Chicago, Illinois 60607, United States;* orcid.org/0000-0003-3124-3235

Andres Ruiz Belmonte − *Department of Chemical and Biological Engineering, Illinois Institute of Technology, Chicago, Illinois 60616, United States*

Jialiang Wei − *Department of Mechanical, Materials, and Aerospace Engineering, Illinois Institute of Technology, Chicago, Illinois 60616, United States*

Kamil Kucuk − *Department of Physics and CSRRI, Illinois Institute of Technology, Chicago, Illinois 60616, United States;* orcid.org/0000-0002-7356-9754

Shubhada Mahesh Khanvilkar − *Department of Chemical and Biological Engineering, Illinois Institute of Technology, Chicago, Illinois 60616, United States*

Erin Efimoff − *Department of Chemical and Biological Engineering, Illinois Institute of Technology, Chicago, Illinois 60616, United States*

Wei Chen − *Department of Mechanical, Materials, and Aerospace Engineering, Illinois Institute of Technology, Chicago, Illinois 60616, United States*

Carlo U. Segre − *Department of Physics and CSRRI, Illinois Institute of Technology, Chicago, Illinois 60616, United States;* orcid.org/0000-0001-7664-1574

Reza Shahbazian-Yassar − *Department of Mechanical and Industrial Engineering, University of Illinois at Chicago, Chicago, Illinois 60607, United States;* orcid.org/0000-0002-7744-4780

Complete contact information is available at: https://pubs.acs.org/10.1021/acsnano.9b08792

Author Contributions

[⊥]These authors equally contributed to this work. M.A. and M.E. conceived the idea of the study. M.E. synthesized the nanoparticles. M.E., A.K., A.R.B., S.M.K., and E.E. performed the electrochemical experiments. M.E. and A.K. performed the XRD, XPS, UPS, and *in situ* Raman characterizations. K.K. performed FESEM characterization. C.U.S. performed XAS experiments. R.S.Y. and B.S. performed the HRTEM characterization. W.C. and J.W. performed DFT calculations. M.A. supervised M.E., A.K., A.R.B., S.M.K., and E.E. efforts.

Notes

The authors declare no competing financial interest.

ACKNOWLEDGMENTS

M.A. was supported by Illinois Institute of Technology start-up funding, Wanger Institute for Sustainable Energy Research (WISER) seed fund (262029 221E 2300), and the Soft and Hybrid Nanotechnology Experimental (SHyNE) Resource seed funding at Northwestern University. R.S.-Y. and B.S. were supported by NSF (DMR-1809439). We acknowledge the MRSEC Materials Preparation and Measurement Laboratory shared user facility at the University of Chicago (NSF DMR-1420709), the EPIC facility (NUANCE Center, Northwestern University), which has received support from the MRSEC program (NSF DMR-1121262) at the Materials Research Center, the Nanoscale Science and Engineering Center (NSF EEC-0647560) at the International Institute for Nanotechnology, and the State of Illinois, through the International Institute for Nanotechnology. The authors acknowledge Dr. Rao Tatavarti from Micro-Link Device, Inc. in Chicago for providing the triple junction PV cell. This work made use of instruments in the Electron Microscopy Service (Research Resources Center, UIC). The acquisition of the UIC JEOL JEM-ARM200CF was supported by an MRI-R2 grant from the National Science Foundation (award no. DMR-0959470).

MRCAT operations are supported by the Department of Energy and the MRCAT member institutions. This research used resources of the Advanced Photon Source and the Center for Nanoscale Materials U.S. Department of Energy (DOE) Office of Science User Facilities operated for the DOE Office of Science by Argonne National Laboratory under contract no. DE-AC02-06CH11357.

REFERENCES

(1) Gielen, D.; Boshell, F.; Saygin, D. Climate and Energy Challenges for Materials Science. *Nat. Mater.* **2016**, *15*, 117.
(2) Moriarty, P.; Honnery, D. Can Renewable Energy Power the Future? *Energy Policy* **2016**, *93*, 3−7.
(3) Chu, S.; Cui, Y.; Liu, N. The Path towards Sustainable Energy. *Nat. Mater.* **2017**, *16*, 16−22.
(4) Asadi, M.; Motevaselian, M. H.; Moradzadeh, A.; Majidi, L.; Esmaeilirad, M.; Sun, T. V.; Liu, C.; Bose, R.; Abbasi, P.; Zapol, P.; Khodadoust, A. P.; Curtiss, L. A.; Aluru, N. R.; Salehi-Khojin, A. Highly Efficient Solar-Driven Carbon Dioxide Reduction on Molybdenum Disulfide Catalyst Using Choline Chloride-Based Electrolyte. *Adv. Eng. Mater.* **2019**, *9*, 1803536.
(5) Montoya, J. H.; Seitz, L. C.; Chakthranont, P.; Vojvodic, A.; Jaramillo, T. F.; Nørskov, J. K. Materials for Solar Fuels and Chemicals. *Nat. Mater.* **2017**, *16*, 70−81.
(6) Wu, J.; Ma, S.; Sun, J.; Gold, J. I.; Tiwary, C.; Kim, B.; Zhu, L.; Chopra, N.; Odeh, I. N.; Vajtai, R.; Yu, A. Z.; Luo, R.; Lou, J.; Ding, G.; et al. A Metal-Free Electrocatalyst for Carbon Dioxide Reduction to Multi-Carbon Hydrocarbons and Oxygenates. *Nat. Commun.* **2016**, *7*, 13869.
(7) Simón-Manso, E.; Kubiak, C. P. Dinuclear Nickel Complexes as Catalysts for Electrochemical Reduction of Carbon Dioxide. *Organometallics* **2005**, *24*, 96−102.
(8) Salehi-Khojin, A.; Jhong, H.-R. M. R. M.; Rosen, B. A.; Zhu, W.; Ma, S.; Kenis, P. J. A.; Masel, R. I. Nanoparticle Silver Catalysts That Show Enhanced Activity for Carbon Dioxide Electrolysis. *J. Phys. Chem. C* **2013**, *117*, 1627−1632.
(9) Whipple, D. T.; Kenis, P. J. A. Prospects of CO_2 Utilization *via* Direct Heterogeneous Electrochemical Reduction. *J. Phys. Chem. Lett.* **2010**, *1*, 3451−3458.
(10) Asadi, M.; Kim, K.; Liu, C.; Addepalli, A. V.; Abbasi, P.; Yasaei, P.; Phillips, P.; Behranginia, A.; Cerrato, J. M.; Haasch, R.; Zapol, P.; Kumar, B.; Klie, R. F.; Abiade, J.; Curtiss, L. A.; Salehi-Khojin, A. Nanostructured Transition Metal Dichalcogenide Electrocatalysts for CO_2 Reduction in Ionic Liquid. *Science* **2016**, *353*, 467−470.
(11) Nocera, D. G. Solar Fuels and Solar Chemicals Industry. *Acc. Chem. Res.* **2017**, *50*, 616−619.
(12) Gao, S.; Lin, Y.; Jiao, X.; Sun, Y.; Luo, Q.; Zhang, W.; Li, D.; Yang, J.; Xie, Y. Partially Oxidized Atomic Cobalt Layers for Carbon Dioxide Electroreduction to Liquid Fuel. *Nature* **2016**, *529*, 68−71.
(13) Liu, M.; Pang, Y.; Zhang, B.; De Luna, P.; Voznyy, O.; Xu, J.; Zheng, X.; Dinh, C. T.; Fan, F.; Cao, C.; Garcia de Arquer, F. P.; Saberi Safaei, T.; Mepham, A.; Klinkova, A.; Kumacheva, E.; Filleter, T.; Sinton, A.; Kelley, S. O.; Sargent, E. H. Enhanced Electrocatalytic CO_2 Reduction *via* Field-Induced Reagent Concentration. *Nature* **2016**, *537*, 382−386.
(14) Kumari, G.; Zhang, X.; Devasia, D.; Heo, J.; Jain, P. K. Watching Visible Light-Driven CO_2 Reduction on a Plasmonic Nanoparticle Catalyst. *ACS Nano* **2018**, *12*, 8330−8340.
(15) Wu, J.; Yadav, R. M.; Liu, M.; Sharma, P. P.; Tiwary, C. S.; Ma, L.; Zou, X.; Zhou, X.; Yakobson, B. I.; Lou, J.; Ajayan, P. M. Achieving Highly Efficient Selective and Stable CO_2 Reduction on Nitrogen-Doped Carbon Nanotubes. *ACS Nano* **2015**, *9*, 5364−5371.
(16) Duan, Y. X.; Meng, F. L.; Liu, K. H.; Yi, S. S.; Li, S. J.; Yan, J. M.; Jiang, Q. Amorphizing of Cu Nanoparticles toward Highly Efficient and Robust Electrocatalyst for CO_2 Reduction to Liquid Fuels with High Faradaic Efficiencies. *Adv. Mater.* **2018**, *30*, 1706194.
(17) Li, C. W.; Kanan, M. W. CO_2 Reduction at Low Overpotential on Cu Electrodes Resulting from the Reduction of Thick Cu_2O Films. *J. Am. Chem. Soc.* **2012**, *134*, 7231−7234.
(18) Chirizzi, D.; Guascito, M. R.; Filippo, E.; Malitesta, C.; Tepore, A. A Novel Nonenzymatic Amperometric Hydrogen Peroxide Sensor Based on CuO@Cu_2O Nanowires Embedded into Poly(Vinyl Alcohol). *Talanta* **2016**, *147*, 124−131.
(19) Weng, Z.; Jiang, J.; Wu, Y.; Wu, Z.; Guo, X.; Materna, K. L.; Liu, W.; Batista, V. S.; Brudvig, G. W.; Wang, H. Electrochemical CO_2 Reduction to Hydrocarbons on a Heterogeneous Molecular Cu Catalyst in Aqueous Solution. *J. Am. Chem. Soc.* **2016**, *138*, 8076−8079.
(20) Liu, X.; Xiao, J.; Peng, H.; Hong, X.; Chan, K.; Nørskov, J. K. Understanding Trends in Electrochemical Carbon Dioxide Reduction Rates. *Nat. Commun.* **2017**, *8*, 15438.
(21) Gao, D.; Zegkinoglou, I.; Divins, N. J.; Scholten, F.; Sinev, I.; Grosse, P.; Roldan Cuenya, B. Plasma-Activated Copper Nanocube Catalysts for Efficient Carbon Dioxide Electroreduction to Hydrocarbons and Alcohols. *ACS Nano* **2017**, *11*, 4825−4831.
(22) Wang, Z.; Yang, G.; Zhang, Z.; Jin, M.; Yin, Y. Selectivity on Etching: Creation of High-Energy Facets on Copper Nanocrystals for CO_2 Electrochemical Reduction. *ACS Nano* **2016**, *10*, 4559−4564.
(23) MacDonald, G. J. The Future of Methane as an Energy Resource. *Annu. Rev. Energy* **1990**, *15*, 53−83.
(24) Kuhl, K. P.; Cave, E. R.; Abram, D. N.; Jaramillo, T. F. New Insights into the Electrochemical Reduction of Carbon Dioxide on Metallic Copper Surfaces. *Energy Environ. Sci.* **2012**, *5*, 7050−7059.
(25) Manthiram, K.; Beberwyck, B. J.; Alivisatos, A. P. Enhanced Electrochemical Methanation of Carbon Dioxide with a Dispersible Nanoscale Copper Catalyst. *J. Am. Chem. Soc.* **2014**, *136*, 13319−13325.
(26) Ma, S.; Sadakiyo, M.; Heima, M.; Luo, R.; Haasch, R. T.; Gold, J. I.; Yamauchi, M.; Kenis, P. J. A. Electroreduction of Carbon Dioxide to Hydrocarbons Using Bimetallic Cu−Pd Catalysts with Different Mixing Patterns. *J. Am. Chem. Soc.* **2017**, *139*, 47−50.
(27) Gattrell, M.; Gupta, N.; Co, A. C. A Review of the Aqueous Electrochemical Reduction of CO_2 to Hydrocarbons at Copper. *J. Electroanal. Chem.* **2006**, *594*, 1−19.
(28) Guo, L. W.; Du, P. P.; Fu, X. P.; Ma, C.; Zeng, J.; Si, R.; Huang, Y. Y.; Jia, C. J.; Zhang, Y. W.; Yan, C. H. Contributions of Distinct Gold Species to Catalytic Reactivity for Carbon Monoxide Oxidation. *Nat. Commun.* **2016**, *7*, 13481.
(29) Zhang, S.; Nguyen, L.; Liang, J. X.; Shan, J.; Liu, J.; Frenkel, A. I.; Patlolla, A.; Huang, W.; Li, J.; Tao, F. Catalysis on Singly Dispersed Bimetallic Sites. *Nat. Commun.* **2015**, *6*, 7938.
(30) Murdoch, M.; Waterhouse, G. I. N.; Nadeem, M. A.; Metson, J. B.; Keane, M. A.; Howe, R. F.; Llorca, J.; Idriss, H. The Effect of Gold Loading and Particle Size on Photocatalytic Hydrogen Production from Ethanol over Au/TiO_2 Nanoparticles. *Nat. Chem.* **2011**, *3*, 489−492.
(31) Serpell, C. J.; Cookson, J.; Ozkaya, D.; Beer, P. D. Core@shell Bimetallic Nanoparticle Synthesis *via* Anion Coordination. *Nat. Chem.* **2011**, *3*, 478−483.
(32) Esmaeilirad, M.; Zabihi, M.; Shayegan, J.; Khorasheh, F. Oxidation of Toluene in Humid Air by Metal Oxides Supported on γ-Alumina. *J. Hazard. Mater.* **2017**, *333*, 293−307.
(33) Huang, M.; Zhang, Y.; Li, F.; Wang, Z.; Alamusi; Hu, N.; Wen, Z.; Liu, Q. Merging of Kirkendall Growth and Ostwald Ripening: CuO@MnO_2 Core-Shell Architectures for Asymmetric Supercapacitors. *Sci. Rep.* **2015**, *4*, 4518.
(34) Schreier, M.; Héroguel, F.; Steier, L.; Ahmad, S.; Luterbacher, J. S.; Mayer, M. T.; Luo, J.; Grätzel, M. Solar Conversion of CO_2 to CO Using Earth-Abundant Electrocatalysts Prepared by Atomic Layer Modification of CuO. *Nat. Energy* **2017**, *2*, 17087.
(35) Tahir, D.; Tougaard, S. Electronic and Optical Properties of Cu, CuO and Cu_2O Studied by Electron Spectroscopy. *J. Phys.: Condens. Matter* **2012**, *24*, 175002.

https://dx.doi.org/10.1021/acsnano.9b08792
ACS Nano 2020, 14, 2099−2108

(36) Yin, M.; Wu, C.; Lou, Y.; Burda, C.; Koberstein, J. T.; Zhu, Y.; O'Brien, S. Copper Oxide Nanocrystals. *J. Am. Chem. Soc.* **2005**, *127*, 9506−9511.
(37) Park, J. C.; Kim, J.; Kwon, H.; Song, H. Gram-Scale Synthesis of Cu_2O Nanocubes and Subsequent Oxidation to CuO Hollow Nanostructures for Lithium-Ion Battery Anode Materials. *Adv. Mater.* **2009**, *21*, 803−807.
(38) Hansen, B. J.; Lu, G.; Chen, J. Direct Oxidation Growth of CuO Nanowires from Copper-Containing Substrates. *J. Nanomater.* **2008**, *2008*, 830474.
(39) Fu, S.; Hsu, Y.; Chen, M.; Chuang, C.; Chen, Y.; Lin, Y. Silver-Decorated Hierarchical Cuprous Oxide Micro/Nanospheres as Highly Effective Surface-Enhanced Raman Scattering Substrates. *Opt. Express* **2014**, *22*, 14617−14624.
(40) Su, D.; Xie, X.; Dou, S.; Wang, G. CuO Single Crystal with Exposed {001} Facets - A Highly Efficient Material for Gas Sensing and Li-Ion Battery Applications. *Sci. Rep.* **2015**, *4*, 5753.
(41) Wang, Q.; Zhang, Y.; Zheng, J.; Wang, Y.; Hu, T.; Meng, C. Metal Oxide Decorated Layered Silicate Magadiite for Enhanced Properties: Insight from ZnO and CuO Decoration. *Dalt. Trans.* **2017**, *46*, 4303−4316.
(42) Zhang, Y. X.; Kuang, M.; Wang, J. J. Mesoporous CuO−NiO Micropolyhedrons: Facile Synthesis, Morphological Evolution and Pseudocapcitive Performance. *CrystEngComm* **2014**, *16*, 492−498.
(43) Asadi, M.; Kim, K.; Liu, C.; Addepalli, A. V.; Abbasi, P.; Yasaei, P.; Phillips, P.; Behranginia, A.; Cerrato, J. M.; Haasch, R.; Zapol, P.; Kumar, B.; Klie, R. F.; Abiade, J.; Curtiss, L. A.; Salehi-Khojin, A. Nanostructured Transition Metal Dichalcogenide Electrocatalysts for CO_2 Reduction in Ionic Liquid. *Science* **2016**, *353*, 467−470.
(44) Li, D. J.; Maiti, U. N.; Lim, J.; Choi, D. S.; Lee, W. J.; Oh, Y.; Lee, G. Y.; Kim, S. O. Molybdenum Sulfide/N-Doped CNT Forest Hybrid Catalysts for High-Performance Hydrogen Evolution Reaction. *Nano Lett.* **2014**, *14*, 1228−1233.
(45) Kim, S. K.; Zhang, Y.; Bergstrom, H.; Michalsky, R.; Peterson, A. Understanding the Low-Overpotential Production of CH_4 from CO_2 on Mo_2C Catalysts. *ACS Catal.* **2016**, *6*, 2003−2013.
(46) Hori, Y.; Murata, A.; Takahashi, R. Formation of Hydrocarbons in the Electrochemical Reduction of Carbon Dioxide at a Copper Electrode in Aqueous Solution. *J. Chem. Soc., Faraday Trans. 1* **1989**, *85*, 2309−2326.
(47) Rosen, B. A.; Zhu, W.; Kaul, G.; Salehi-Khojin, A.; Masel, R. I. Water Enhancement of CO_2 Conversion on Silver in 1-Ethyl-3-Methylimidazolium Tetrafluoroborate. *J. Electrochem. Soc.* **2013**, *160*, H138−H141.
(48) Sun, Z.; Ma, T.; Tao, H.; Fan, Q.; Han, B. Fundamentals and Challenges of Electrochemical CO_2 Reduction Using Two-Dimensional Materials. *CHEMPR* **2017**, *3*, 560−587.
(49) Kuhl, K. P.; Hatsukade, T.; Cave, E. R.; Abram, D. N.; Kibsgaard, J.; Jaramillo, T. F. Electrocatalytic Conversion of Carbon Dioxide to Methane and Methanol on Transition Metal Surfaces. *J. Am. Chem. Soc.* **2014**, *136*, 14107−14113.
(50) Kondori, A.; Esmaeilirad, M.; Baskin, A.; Song, B.; Wei, J.; Chen, W.; Segre, C. U.; Shahbazian-Yassar, R.; Prendergast, D.; Asadi, M. Identifying Catalytic Active Sites of Trimolybdenum Phosphide (Mo_3P) for Electrochemical Hydrogen Evolution. *Adv. Energy Mater.* **2019**, *9*, 1900516.
(51) Choi, Y.; Liu, P. Mechanism of Ethanol Synthesis from Syngas on Rh (111). *J. Am. Chem. Soc.* **2009**, *131*, 13054−13061.
(52) Remediakis, I. N.; Abild-Pedersen, F.; Nørskov, J. K. DFT Study of Formaldehyde and Methanol Synthesis from CO and H_2 on Ni (111). *J. Phys. Chem. B* **2004**, *108*, 14535−14540.
(53) Kropf, A. J.; Katsoudas, J.; Chattopadhyay, S.; Shibata, T.; Lang, E. A.; Zyryanov, V. N.; Ravel, B.; McIvor, K.; Kemner, K. M.; Scheckel, k. G.; Bare, K. G.; Terry, J.; Kelly, S. D.; Bunker, B. A.; Segre, C. U.; et al. The New MRCAT (Sector 10) Bending Magnet Beamline at the Advanced Photon Source. *AIP Conf. Proc.* **2009**, *1234*, 299−302.
(54) Ravel, B.; Newville, M. ATHENA, ARTEMIS, HEPHAESTUS: Data Analysis for X-Ray Absorption Spectroscopy Using IFEFFIT. *J. Synchrotron Radiat.* **2005**, *12*, 537−541.
(55) Newville, M. IFEFFIT: Interactive XAFS Anaysis and FEFF Fitting. *J. Synchrotron Radiat.* **2001**, *8*, 322−324.
(56) Kresse, G.; Joubert, D. From Ultrasoft Pseudopotentials to the Projector Augmented-Wave Method. *Phys. Rev. B: Condens. Matter Mater. Phys.* **1999**, *59*, 1758−1775.
(57) Jain, A.; Ong, S. P.; Hautier, G.; Chen, W.; Richards, W. D.; Dacek, S.; Cholia, S.; Gunter, D.; Skinner, D.; Ceder, G.; Persson, K. A. Commentary: The Materials Project: A Materials Genome Approach to Accelerating Materials Innovation. *APL Mater.* **2013**, *1*, 011002.
(58) Ong, S. P.; Richards, W. D.; Jain, A.; Hautier, G.; Kocher, M.; Cholia, S.; Gunter, D.; Chevrier, V. L.; Persson, K. A.; Ceder, G. Python Materials Genomics (Pymatgen): A Robust, Open-Source Python Library for Materials Analysis. *Comput. Mater. Sci.* **2013**, *68*, 314−319.

https://dx.doi.org/10.1021/acsnano.9b08792
ACS Nano 2020, 14, 2099−2108